Infrasound signal detection and characterization using ground-coupled airwaves on a single seismo-acoustic sensor pair

Kathleen McKee[1] (kfmckee@alaska.edu), David Fee[1], Matthew Haney[2], John Lyons[2], Robin Matoza[3]

[1]Geophysical Institute, Alaska Volcano Observatory, University of Alaska Fairbanks, [2]Alaska Volcano Observatory, U.S. Geological Survey, [3]Department of Earth Science, University of California, Santa Barbara

Research Question

Can we find back-azimuth to an infrasonic source using seismo-acoustic data from a nearly collocated seismometer and microphone? How robust is the technique?

Motivation & Key Points

- A single seismo-acoustic station is more economical than an array of microphones or seismometers
- Deploying a microphone with a seismometer enables distinguishing subsurface from subaerial sources
- Separating the microphone and seismometer by 10s of meters makes the wind noise incoherent
- Infrasound and ground-coupled airwave traces have 90 degree phase
- Back-azimuth determined with 2 microphones produces non-unique solution. By replacing one microphone with a 3-component seismometer, we aim to determine a unique solution by integrating particle motion.

Ground-coupled Airwaves (GCA) Primer

Figure 1

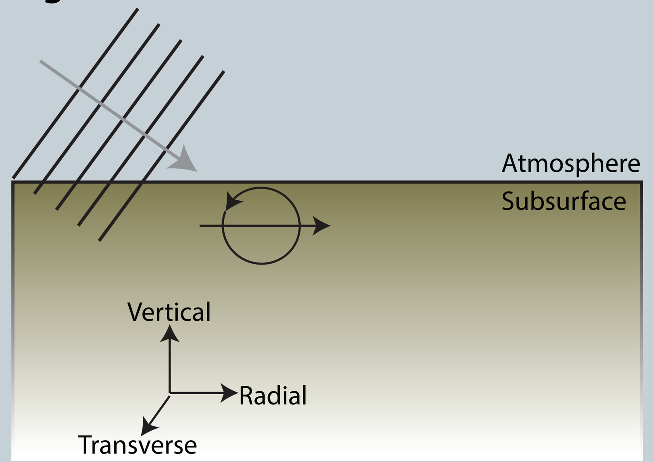

Figure 2

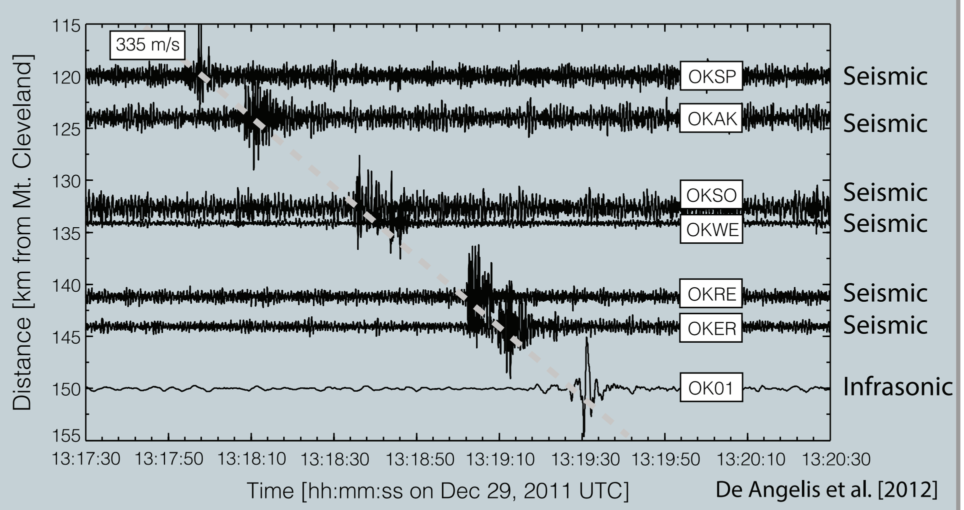

- Acoustic wave shakes the ground
- Ground shaking propagates as a Rayleigh surface wave
- Rayleigh waves have retrograde particle motion

- Seismometers are sensitive to Rayleigh waves in the vertical and radial components
- GCAs travel at the speed of sound in the atmosphere ~343 m/s

Determining signal from wind noise

Pressure change on ground surface

$$P(t,x_p) = p_{in}(t,x_p) + H_{wp}w_{in}(t,x_p) + N_p(t,x_p)$$

Incident pressure wave; Ground-air coupling; Wind noise

Vertical velocity observed

$$W(t,x_s) = w_{in}(t,x_s) + H_{pw}p_{in}(t,x_s) + H^n_{pw}N_p(t,x_s)$$

Incident Rayleigh wave; Air-ground coupling; Wind noise coupled to ground

Coefficient for P to produce W

90˚ phase

$$H_{pw} = \frac{e^{-i\pi/2}c_a}{2(\lambda+\mu)}\frac{\lambda+2\mu}{\mu}$$

Cross correlation yields:

$$R[\tau; W, P] \sim R[\tau; w_{in}, p_{in}] + R[\tau; w_{in}, H_{wp}w_{in}] + R[\tau; H_{pw}p_{in}, p_{in}]$$

Ichihara et al. [2012]

Figure 3

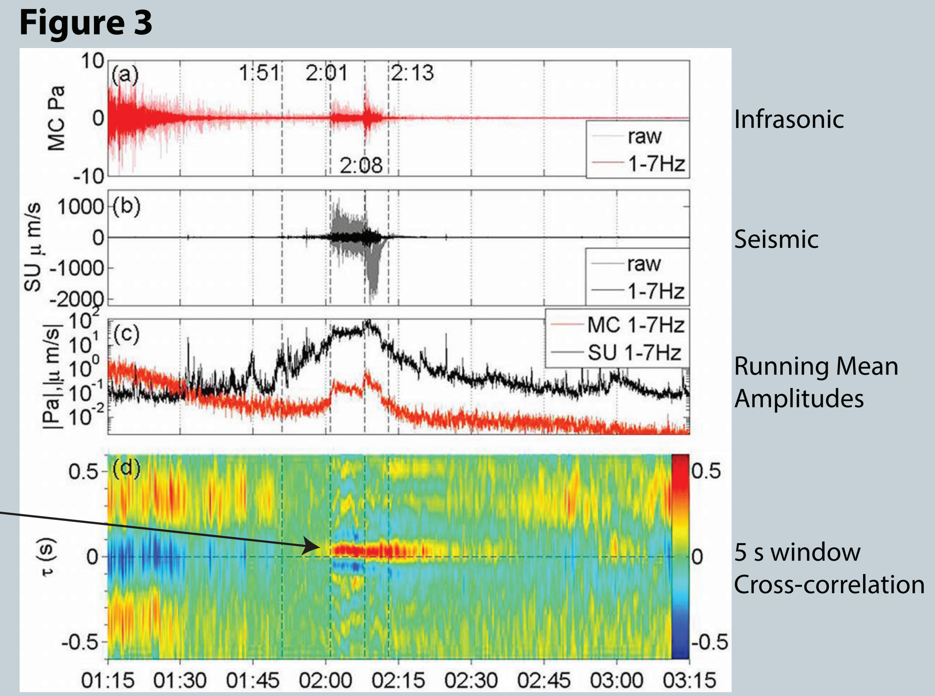

The Forward Problem

- Knowns: Source, microphone and seismometer locations
- Use the known apparent distance, d_a, to shift the seismic (or infrasonic) waveform in time to account for additional travel time.
- After shifting the data, the characteristic 90˚ phase should appear in the phase spectrogram (or phase-o-gram) as in Fig. 5 f.

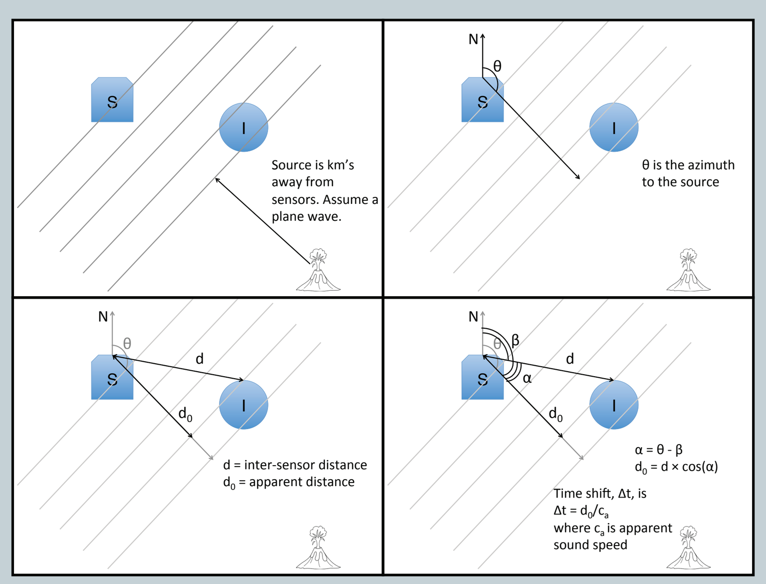

Figure 4 Forward Problem: Method for shifting the data to correct for apparent distance and highlight the 90 degree phase.

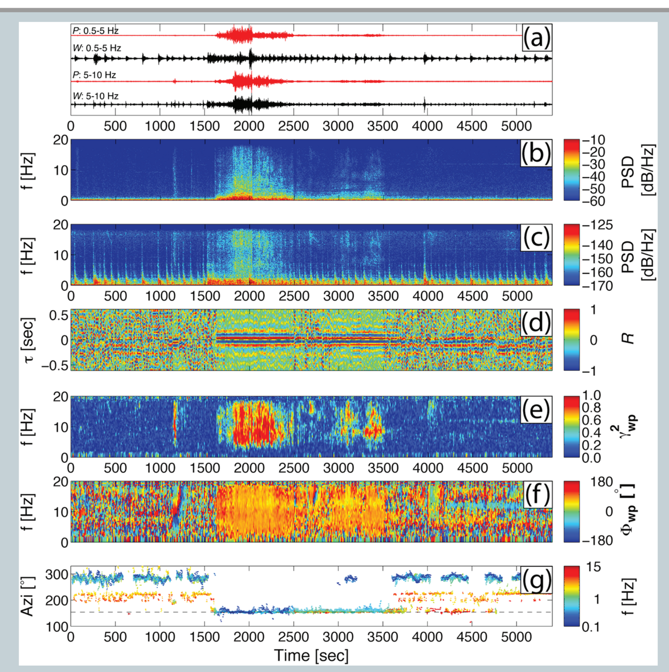

Figure 5 (a) Infrasound (red) and seismic (black) waveforms; (b) Infrasound and (b) seismic spectrograms; (d) Cross-correlation between infrasound and seismic waveforms; (e) Cohere-o-gram; (f) Phase-o-gram; (g) Azimuth to source using array processing

- Determining the seismo-acoustic coherence through time (a.k.a. cohere-o-gram) shows when and at what frequencies the signals are similar.

The Inverse Problem

Here we use synthetic seismic and acoustic data to investigate the inverse problem (Fig. 6). The synthetic data are generated by a coupled Earth-atmosphere 3D finite difference code (Figs. 7 & 8) (Haney et al. [2009]).

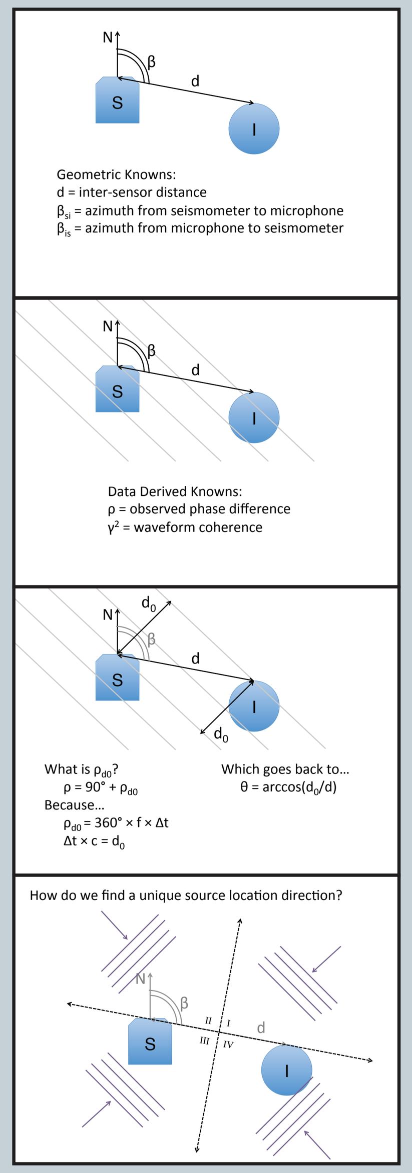

Figure 6 Inverse Method

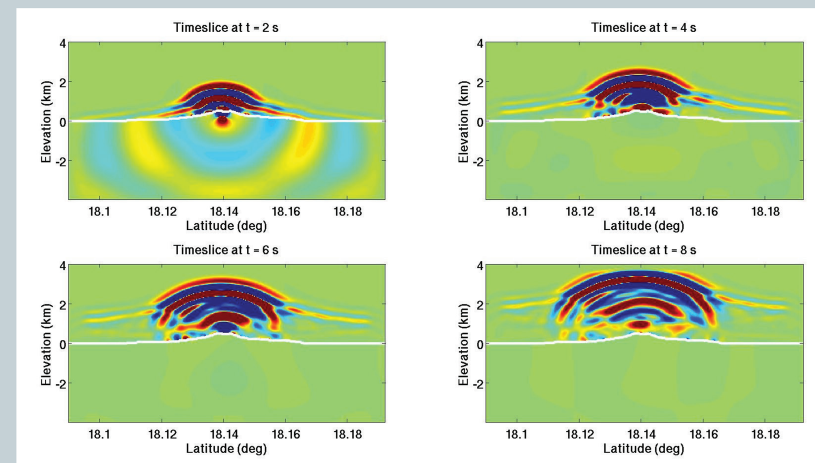

Figure 7 Time slices of the simulation from Earth-atmosphere 3D finite difference code using topography from Pagan Volcano. At t = 2 s, the seismic wave passes and couples to the atmosphere. At t = 6 s, the acoustic wave passes and couples to the earth.

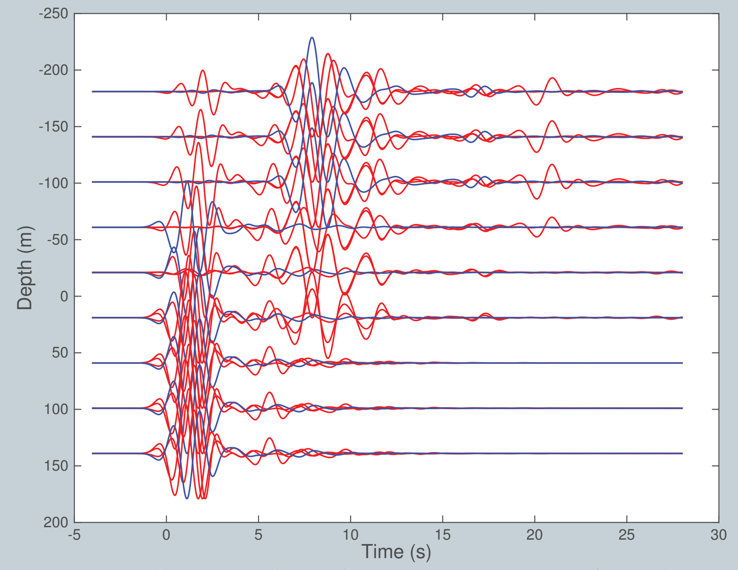

Figure 8 Synthetic waveforms for three components of particle velocity (red) and 1 component of pressure (blue) at 9 difference depths. Positive values are subsurface and negative values are subaerial. Station PGBF is at 21 m elevation.

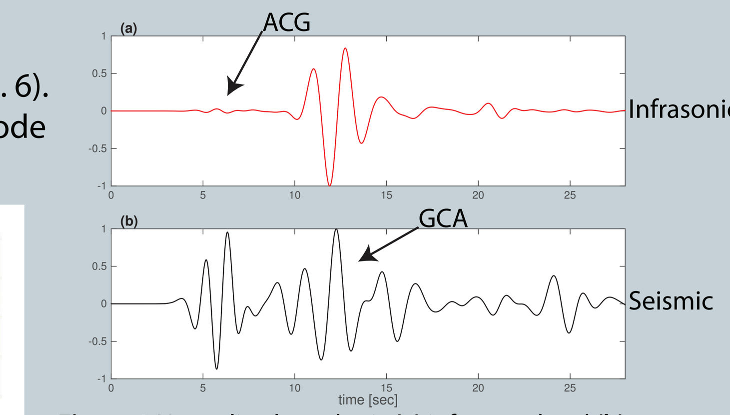

Figure 9 Normalized, synthetic (a) infrasound and (b) vertical seismic traces. The seismic signal arrives first, ~4 sec, and shows up on the infrasound trace as an air-coupled ground-wave (ACG). The explosion airwave arrives at ~9 sec in the infrasound and shows up on seismic trace as a GCA. Both the ACG and GCA have a phase shift from the seismic and infrasonic signals, respectively.

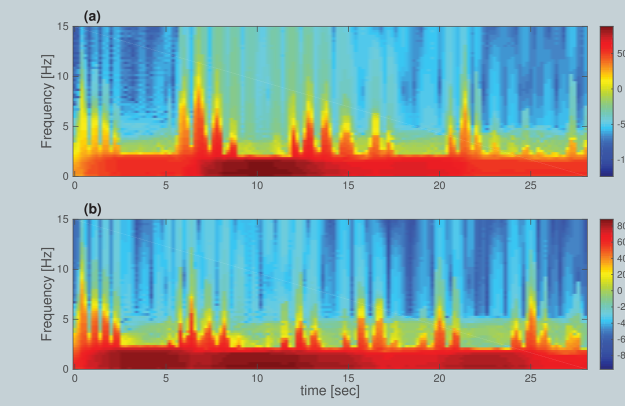

Figure 10 (a) Infrasound and (b) seismic spectrograms. For both, most of the energy is below about 5 Hz. These were calculated using the multitaper method.

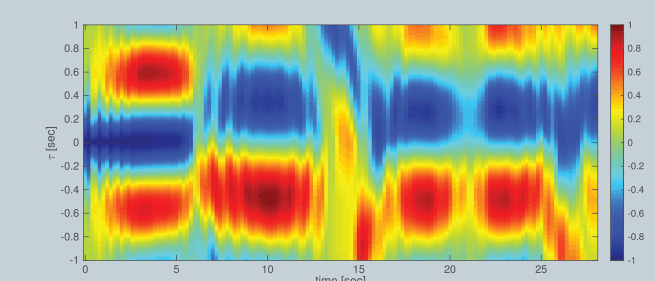

Figure 11 Cross-correlation between seismic and infrasound. At ~10 sec the time shift/phase between the infrasound and GCA is observed.

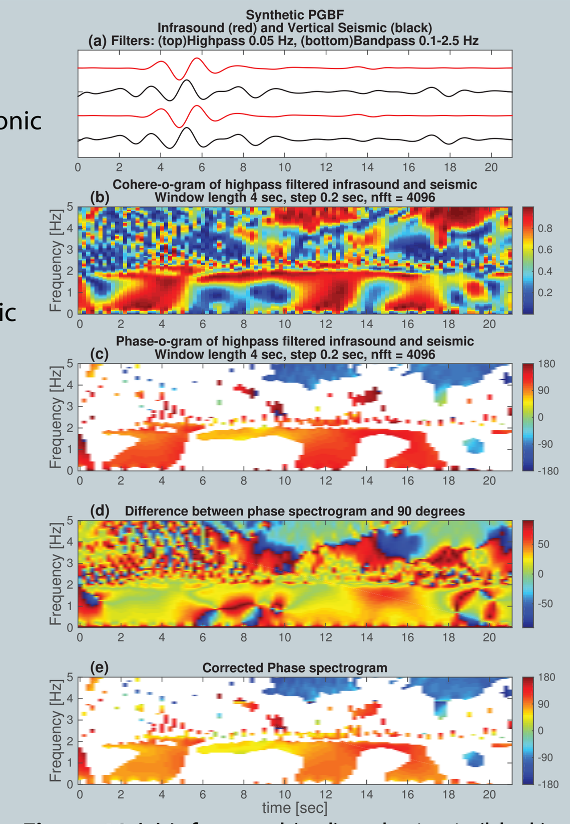

Figure 12 (a) Infrasound (red) and seismic (black); (b) Cohere-o-gram (coherence spectra); (c) Phase-o-gram (phase spectrogram); times with coherence below 0.7 are whited out. (d) This plots the difference between the phase-o-gram and 90 degrees. (e) 'Corrected' phase-o-gram.

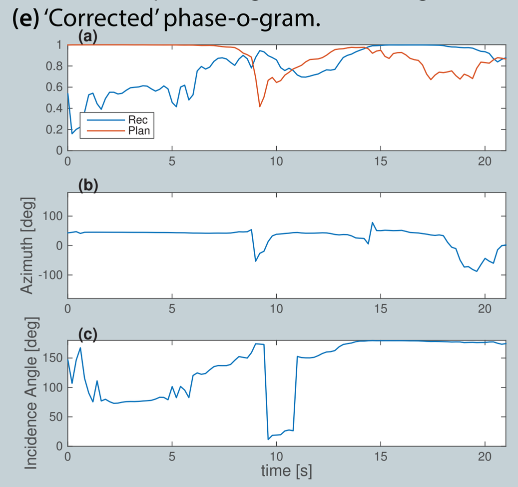

Figure 13 (a) Rectilinearity (blue) and Planarity (red) of synthetic seismic data through time. (b) Azimuth of wave propagation direction through time. (c) Angle of incidence through time.

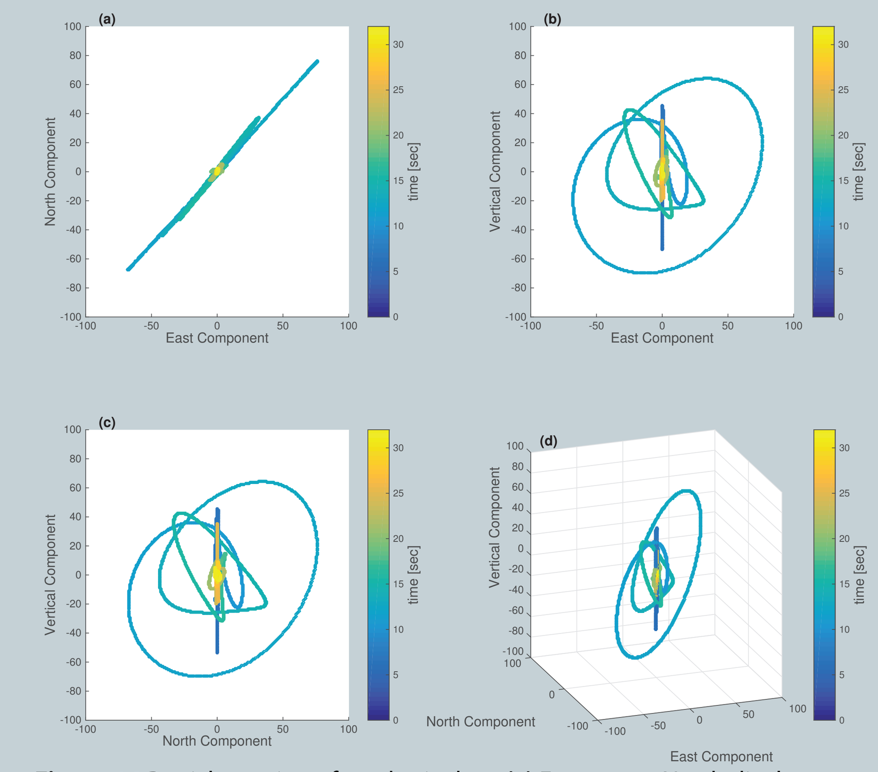

Figure 14 Particle motion of synthetic data. (a) East versus North displacement; (b) East versus Vertical displacement; (c) North versus Vertical displacement; (d) East versus North versus Vertical displacement. Time is noted by the color.

Highlights:

- Figure 7 shows air-coupled ground wave and ground-coupled airwave
- Figure 11 shows characteristic lag in cross-correlation of GCA and infrasound
- Figure 12 highlights high coherence between GCA and infrasound and shows the 90 phase between them
- Figure 13 Show high planarity and low rectilinearity during GCA and an azimuth of ~45 deg
- Figure 14 shows Rayleigh-wave like particle motion pointing in the direction of the synthetic source

Application

- Fig. 16: an example of a GCA from an explosion at Pagan with high coherence and 90 deg. phase knowing the source location
- Fig. 17: Phase is corrected to 90 degrees without source location
- Fig. 18: Rectilinearity, planarity and resulting azimuth and incidence angle are inconclusive
- Fig. 19: Scatter in subplots suggest Rayleigh wave-like particle motion, but more investigation is needed

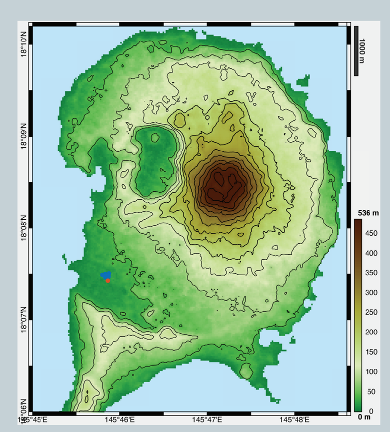

Figure 15 Topographic map of Pagan Volcano, Northern Mariana Islands. Station PGBF is noted by the red (seismic) and blue (infrasound) dots.

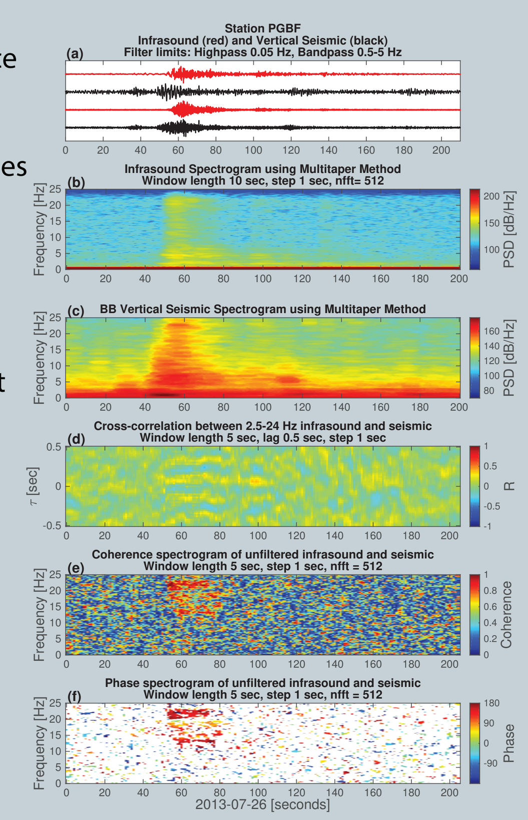

Figure 16 Forward Problem (a) Waveforms; (b) Infrasound spectrogram; (c) seismic spectrogram; (d) Cross-correlation between seismic and infrasound; (e) Cohere-o-gram; (f) Corrected Phase-o-gram using volcano location.

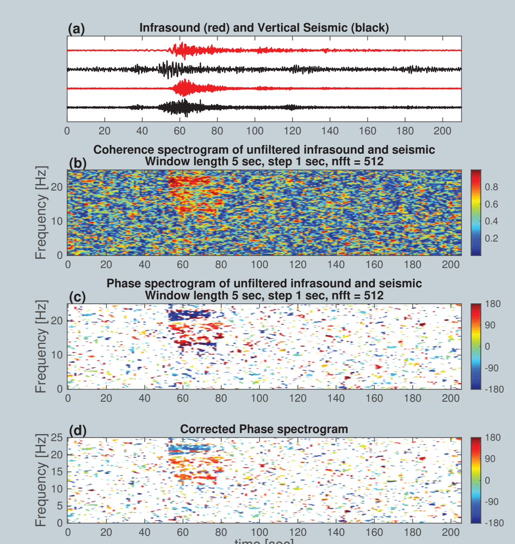

Figure 17 Inverse Problem (a) Waveforms; (b) Cohere-o-gram; (c) Phase-o-gram; (d) Corrected Phase-o-gram.

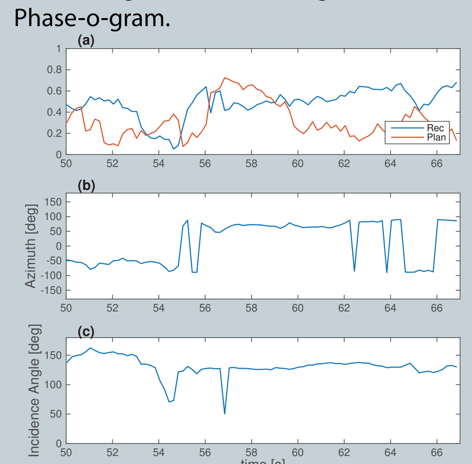

Figure 18 (a) Rectilinearity (blue) and Planarity (red) of synthetic seismic data through time. (b) Azimuth of wave propagation direction through time. (c) Angle of incidence through time.

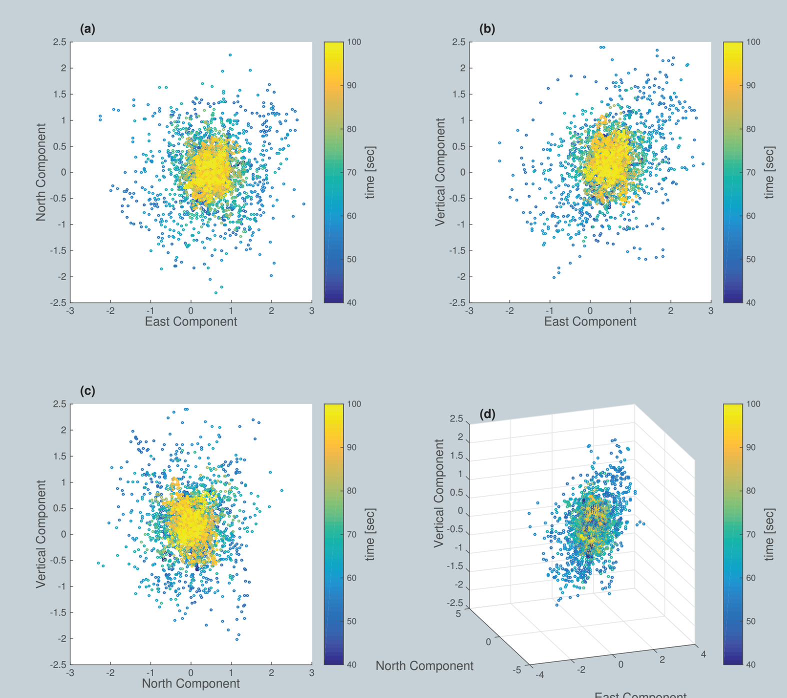

Figure 19 Particle motion of synthetic data. (a) East versus North displacement; (b) East versus Vertical displacement; (c) North versus Vertical displacement; (d) East versus North versus Vertical displacement. Time is noted by the color.

Preliminary results

- We observe the characteristic phase delay between seismic and infrasound synthetic waveforms in the cross-correlation and phase-o-gram
- Synthetic acoustic and GCA data show coherence and retrograde particle motion
- Pagan explosion shows coherence and phase between the seismic and acoustic traces
- Pagan data show Rayleigh wave-like particle motion

Next Steps

- Test separation distances with synthetic data
- Add noise (white and pink) to synthetic data and test method at various SNRs
- Test methodology with other data sets: Chelyabinsk meteor; and Pagan, Cleveland, Pavlof and Calbuco Volcanoes

References

Ben-Menahem, A. and Singh, S.J., 1981. Seismic Waves and Sources. Springer, New York.
De Angelis, S., Fee, D., Haney, M. and Schneider, D., 2012. Detecting hidden volcanic explosions from Mt. Cleveland Volcano, Alaska with infrasound and ground-coupled airwaves. Geophysical Research Letters, 39(L21312). doi: 10.1029/2012gl053635
Edwards, W.N., Eaton, D.W., McCausland, P.J., ReVelle, D.O. and Brown, P.G., 2007. Calibrating infrasonic to seismic coupling using the Stardust sample return capsule shockwave: Implications for seismic observations of meteors. Journal of Geophysical Research: Solid Earth (1978–2012), 112(B10). doi: 10.1029/2006JB004621
Ereditato, D. and Luongo, G., 1994. Volcanic tremor wave field during quiescent and eruptive activity at Mt. Etna (Sicily). Journal of Volcanology and Geothermal Research, 61: 239-251.
Haney, M.M., van Wijk, K., Preston, L.A. and Aldridge, D.F., 2009. Observation and modeling of source effects in coda wave interferometry at Pavlof volcano. The Leading Edge, 28(5): 554-560. doi: 10.1190/1.3124930
Ichihara, M., Takeo, M., Yokoo, A., Oikawa, J. and Ohminato, T., 2012. Monitoring volcanic activity using correlation patterns between infrasound and ground motion. Geophysical Research Letters, 39(4). doi: 10.1029/2011gl050542
Lyons, J.J., Haney, M.M., Werner, C., Kelly, P., Patrick, M., Kern, C. and Trusdell, F., 2016. Long period seismicity and very long period infrasound driven by shallow magmatic degassing at Mount Pagan, Mariana Islands. J. Geophys. Res. Solid Earth, 121(1): 188-209. doi: 10.1002/2015JB012490
Matoza, R.S. and Fee, D., 2014. Infrasonic component of volcano-seismic eruption tremor. Geophysical Research Letters, 41(6): 1964-1970. doi: 10.1002/2014GL059301
Montalbetti, J.F. and Kanasewich, E.R., 1970. Enhancement of Teleseismic Body Phases with a Polarization Filter. Geophysical Journal of the Royal Astronomical Society, 21: 119-129.

Acknowledgements

This work is partially funded by: NSF-EAR 1331084.